Nanostructured tin oxide materials for the sub-ppm detection of indoor formaldehyde pollution

Jean-Baptiste Sanchez, Angela Sanchez-Sanchez, Maria Teresa Izquierdo, Sandrine Mathieu, Jaafar Ghanbaja, Franck Berger, Alain Celzard, Vanessa Fierro

Nanostructured tin oxide materials for the sub-ppm detection of indoor formaldehyde pollution

Jean-Baptiste Sanchez[a, *], Angela Sanchez-Sanchez[b], Maria Teresa Izquierdo[c], Sandrine Mathieu[d], Jaafar Ghanbaja[d], Franck Berger[a], Alain Celzard[b], Vanessa Fierro[b]

a. Institut FEMTO-ST, UMR CNRS 6174, Université Bourgogne Franche-Comté, 15B Avenue des montboucons, 25030 Besançon, France.

b. Institut Jean Lamour, UMR CNRS-Université de Lorraine n°7198, ENSTIB, 27 Rue Philippe Séguin, BP 21042, 88051 Epinal Cedex 9, France.

c. Instituto de Carboquimica, ICB-CSIC, Miguel Luesma Castan, 4, 50018 Zaragoza, Spain.

d. Institut Jean Lamour, UMR CNRS-Université de Lorraine n°7198, 2 allée André Guinier, BP 50840, 54011 Nancy cedex, France.

*Corresponding authors: Jean-Baptiste Sanchez

Abstract: Interesting sensing performances of indoor formaldehyde pollution were obtained when small amounts of zinc were introduced in tin oxides. Nanostructured Sn oxide-based porous materials doped with Zn or not, were synthesized using hydrothermal routes. The physicochemical properties of the as-prepared metal-oxide materials were characterized using nitrogen adsorption, X-ray powder diffraction (XRD), scanning electron microscopy (SEM), transmission electron microscopy (TEM) and X-ray photoelectron spectroscopy (XPS). Gas sensors were prepared using the aforementioned tin oxide materials and they exhibited a high sensitivity to formaldehyde at 230°C, as well as a good repeatability over the time. Their limit of formaldehyde detection was as low as 8 ppb in dry air and 50 ppb in air with 60% RH at 25°C. These results were much better that those reported in the open literature and they were attributed to both higher area BET, around 180 m^2/g, and smaller crystallite size, 3.1 nm.

Keywords: formaldehyde, chemical gas sensor, nanoporous material, tin oxide, indoor air pollution

1. Introduction

Ambient air quality within buildings is considered as a major public health concern. Among the many chemicals that can be found in indoor air, formaldehyde is considered as one of the most toxic volatile organic compounds (VOC) [1, 2]. Emissions of formaldehyde essentially originate from furniture made of agglomerated wood (plywood panels, fiberboards, oriented strand boards, etc.), which slowly releases unreacted formaldehyde from the adhesive, but also from textiles, paints, cleaning products and cosmetics [3, 4]. In the early 2000's, formaldehyde has been classified carcinogenic, mutagenic and reprotoxic (CMR) by the International Agency for Research on Cancer (IARC) and by the World Health Organization (WHO). Several safety and occupational health authorities worldwide have laid down permissible exposure levels of formaldehyde by inhalation [5]. For example, the French Agency for Environmental and Occupational Health Safety (AFSSET) has estimated the short-term (up to 2 hours) and long-term (above 2 hours) formaldehyde exposure limits to 50 µg m^{-3} (40 ppb) and 10 µg m^{-3} (8 ppb), respectively [6, 7]. These international guideline values are based on results of epidemiological and toxicological test outcomes, obtained from both human and animal, for a certain exposure time or are based on health hazard assessments in the relevant toxicological literature [5].

For monitoring the presence of formaldehyde in indoor air, chemiresistive-type semiconductor-based gas sensors appear as attractive devices due to their small size, fast response, extensive stability with time and easy use [8, 9]. Among metal oxide semiconductors, SnO_2 still remains the leading material for detecting reducing gases due to its good sensitivity and stability [10 -13]. It is also well-known that the sensing performances

of this kind of sensor are directly controlled by grain size, structure, surface area and morphology of SnO_2 materials [14-16].

Over the past few years, many methods were extensively investigated for producing highly porous nanoparticles of SnO_2 with well-adjusted architecture, able to enhance the gas detection performances of metal oxide-based gas sensors [17]. Sol-gel [18], sputtering [19] or chemical precipitation [20] were the most popular techniques reported in the literature. However, and although significant progresses have been made for improving the gas sensing performances of SnO_2-based sensor by morphology control, the detection limit of formaldehyde still remains higher than the recommended exposure levels.

In the present study, an easy and fast hydrothermal method is reported to produce porous SnO_2-based materials for the sub-ppm detection of formaldehyde. Materials were produced by hydrothermal synthesis and were thoroughly characterized in order to obtain information about texture, morphology and composition of the as-prepared tin oxides. Finally, detection performances of the nanoporous SnO_2-based materials were evaluated in the presence of low concentrations of formaldehyde in air containing various levels of relative humidity. We show that the obtained performances in the sub-ppm detection of indoor formaldehyde pollution are in the range of those fixed by the occupational health authorities worldwide.

2. Experimental

2.1. Raw materials

Tin(IV) chloride hydrate ($SnCl_4 \cdot xH_2O$, 98%), and zinc acetate di-hydrate ($Zn(COOCH_3)_2 \cdot 2H_2O$, 97%) were purchased from Alfa Aesar. Sodium hydroxide (97-100%), hydrochloric acid (37%) and absolute ethanol (> 99.9%) were provided by Sigma-Aldrich. All the materials were used as received.

2.2. Preparation of tin oxides

SnO_2 and Zn-doped materials were prepared with a synthesis method inspired by Dou et al. [21]. In this study, we labelled our nanostructured materials NS Sn and NS Zn/Sn for non-doped and Zn-doped Sn oxides, respectively. NS Sn was obtained first by dissolving $SnCl_4$ (0.27 g) and NaOH (0.002 g) in a mixture of distilled water (15 mL) and absolute ethanol (15 mL). The resultant solution was then transferred into a Teflon-lined autoclave (50 mL) and submitted to thermal treatment (180°C). After 24h, the autoclave was opened and the solid product was collected by centrifugation, washed three times with distilled water, and dried at ambient pressure (70°C, 12 h). For obtaining the material doped with Zn (NS Zn/Sn), the same synthesis procedure was applied but with addition of zinc acetate ($Zn(COOCH_3)_2\ 2H_2O$; 0.004 g) to the aqueous solution of $SnCl_4$. Then, we used distilled water instead of deionized water for the synthesis on the one hand, and we washed with distilled water instead of using distilled water and ethanol on the other hand. As shown below, these two apparently very minor differences with respect to the synthesis method used by Dou et al. [21] had a paramount importance on the resultant textural properties of the materials.

2.3. Characterization techniques

Nitrogen adsorption-desorption isotherms were obtained at -196°C using a Micromeritics ASAP 2020 automatic system. For that purpose, the porous tin oxides were outgassed at 60°C under secondary vacuum for at least 48 hours prior to any measurement. The BET area, A_{BET}, was calculated by applying the BET equation [22] to the nitrogen adsorption isotherms. The total pore volume, $V_{0.97}$, was calculated as the amount of nitrogen adsorbed at the relative pressure of 0.97. The micropore volume, $V_{\mu\text{-}N2}$, was calculated by applying the Dubinin-Radushkevich equation [23] to the N_2 isotherms. The mesopore volume, V_{meso}, was calculated by subtracting $V_{\mu\text{-}N2}$ from $V_{0.97}$. Finally, the pore size distributions (PSDs) of the oxides were calculated with the AS1Win software of Quantachrome Instruments, by applying to the adsorption branch of the nitrogen isotherms the Non-Local Density Functional Theory (NLDFT) for silica at equilibrium.

High-angle XRD patterns were collected with a Bruker D8 Advance X-ray powder diffractometer, equipped with a Cu anode as X-ray source (working at 40 kV and 40 mA) and with an energy-dispersive one-dimensional detector. The diffraction patterns were obtained over the 2θ range of 10º to 80º with steps of 0.019º. Crystalline phase assignation was based on Joint Committee on Powder Diffraction Standards (JCPDS) cards. Quantitative XRD analysis was performed by Rietveld refinement applied to the full pattern, using TOPAS software to obtain the average crystallite size of crystalline phases.

Small-angle XRD patterns were collected with a Bruker D8 Advance X-ray powder diffractometer, equipped with a Cu anode as X-ray source (working at 40 kV and 40 mA) and with a scintillation detector. Silver behenate was used as a low-angle diffraction standard calibration for specimen displacement correction, with d_{001} = 583.80 pm.

Scanning Electron Microscopy (SEM) images were obtained with a FEI XL30 SFEG and a FEI Quanta 450W scanning electron microscopes without metallization.

The morphologies and size of the SnO_2 doped and non-doped materials were also obtained from transmission electron microscopy (TEM) measurements, which were carried out using a JEM - ARM 200F Cold FEG TEM/STEM operating at 200 kV and equipped with a spherical aberration (Cs) probe and image correctors (point resolution 0.12 nm in TEM mode and 0.078 nm in STEM mode).

X-ray photoelectron spectroscopy (XPS) data were obtained with an ESCAPlus OMICROM system equipped with a hemispherical electron energy analyser. The spectrometer was operated at 10 kV and 15 mA under vacuum ($< 5 \times 10^{-9}$ Torr), using a non-monochromatized MgKα X-ray source ($h\upsilon$ = 1253.6 eV). Analyser pass energies of 50 and 20 eV were used for survey scans and for detailed scans, respectively. Binding energies were referenced to the C1s peak (284.5 eV) from adventitious carbonaceous contamination. A survey scan (1 sweep / 200 ms dwell) was acquired between 1100 and 0 eV. Current region sweeps for Sn3d, Zn2p, O1s and C1s were obtained. The CASA data processing software allowed smoothing, Shirley-type background subtraction (for metals, Tougaard background subtraction was used), peak fitting, and quantification. The atomic percentages of each element were calculated from intensity ratios using Wagner sensitivity factors [24].

2.4. Preparation of sensors and gas detection measurements

The as-prepared SnO_2 materials were dispersed in ethanol at a concentration equal to 100 mg L^{-1} and then drop-casted onto commercial sensor platforms (Heraeus MSP 632) to obtain thick-film gas sensors. These platforms are made of interdigitated combs and allow the heating, temperature and conductance measurement of the sensitive material as a

function of time. Each thick-film gas sensor was finally inserted inside a 25 ml gas chamber to study their sensing performances. Before the test, each sensor was aged under synthetic air flow (2% relative humidity (RH) at 25°C, 100 mL min^{-1}) at 500°C for 48 h to ensure the crystallization of materials and then the stabilization of the sensors resistance. This synthetic air was used as carrier gas, both for oxide stabilization and for formaldehyde dilution. Formaldehyde vapors were obtained using a permeation oven. The permeation rate of formaldehyde was estimated at 200 ng min^{-1}, thus leading to an initial concentration of formaldehyde equal to 262 ppb in synthetic air.

The gas response of the sensor was defined as $S = G/G°$, where G is the conductance under synthetic air mixed with formaldehyde, and $G°$ is the conductance under pure synthetic air. To evaluate the detection performances of each sensor, the experiments were divided in two groups. Firstly, experiments were carried out in synthetic air with a relative humidity equal to 2% at 25°C in order to determine both the optimum operating temperature and the limit of detection (LOD) of each gas sensor. Secondly, after having identified the best material for formaldehyde detection in synthetic air, additional experiments were carried out in order to evaluate the new LOD in the presence of humidity (60% RH at 25°C).

3. Results and discussion

3.1. Structure and morphology

Fig. 1 (a) displays the nitrogen adsorption-desorption isotherms of the materials at -196°C and Fig. 1 (b) shows the corresponding pore size distributions (PSDs). The isotherms were type IV and possessed hysteresis loops typical of capillary condensation in mesoporous

materials. The nitrogen uptake up to a relative pressure of 0.1 indicates the presence of micropores (pore diameters lower than 2 nm) in both samples. Both materials exhibited H2-type hysteresis loops, typical of ink-bottle pores with network connectivity. The porous texture of the materials was mainly composed of mesopores, corresponding to more than 60% of the total pore volume, although NS Zn/Sn exhibited a lower mesopore volume, 0.10 $cm^3\ g^{-1}$, compared to that of NS Sn, 0.12 $cm^3\ g^{-1}$. Both materials comprised moderate amounts of micropores, 0.06 $cm^3\ g^{-1}$.

NS Sn and NS Zn/Sn exhibited mesopore size distributions centered on a diameter of 5 nm. NS Sn and NS Zn/Sn exhibited similar A_{BET} values, 185 and 177 $m^2\ g^{-1}$, respectively. Table 1 reports some literature data on the textural properties of nanostructured SnO_2 materials synthesized for gas sensing applications. It is noteworthy that the studied SnO_2 materials presented much higher surface areas than those previously reported for SnO_2 synthesized using similar procedures Zn-doping of NS Sn slightly decreased the mesopore volume while keeping the PSD almost unchanged.

XRD patterns and resultant crystallographic data are shown in Fig. 2 (a). The XRD patterns presented bands between 20 and 80° corresponding to the (110), (101), (200), (211), (220), (002), (310), (301), (202) and (321) reflections, which are assigned to the rutile-type of SnO_2 (JCPDS card, no. 41-1445). Tetrahedral lattice constants (a = 474 pm and c = 379 pm) calculated by Rietveld refinement were identical for both materials. These data agree with values already reported for SnO_2 (a = 473 pm and c = 318 pm). Neither peak of compounds other than SnO_2, nor Zn phases in NS Zn/Sn were detected in the XRD patterns. Those facts can be explained: (i) either by the low concentration of the Zn phases; or (ii) by the too small crystallite size of the Zn phases, thus preventing their observation by this technique. The

narrower peaks of the NS Sn pattern indicate that the crystallite size, *D*, is higher than that of the NS Zn/Sn material, as confirmed by the calculations: crystallite sizes were indeed 3.3 $\pm$ 0.02 nm and 3.1 $\pm$ 0.02 nm, respectively. Therefore the main effect of Zn addition was the reduction of the crystallite size.

The chemical nature of the materials surface was studied by X-ray photoelectron spectroscopy (XPS). Fig. 2 (b) and (d) shows the fitting of the O1s high-resolution spectra, which led to two contributions for NS Sn and NS Zn/Sn. Fig. 2 (c) and (e) also displays the binding energy regimes containing the $Sn3d_{3/2}$ and $Sn3d_{5/2}$ emission lines of the materials. Calculations for the $Sn3d_{3/2}$ and $Sn3d_{5/2}$ orbitals yielded a peak area ratio near the corresponding 0.66 for the 3d orbital. The position of the $Sn3d_{3/2}$ line was found 8.4 eV higher than the binding energy of the $Sn3d_{5/2}$ line, and the symmetry of the peaks for all the samples indicated the absence of metallic Sn. The position of the $Sn3d_{5/2}$ line indicated the presence of oxidized Sn species, in particular SnO_2. These results agree with the XRD results presented above. Binding energies (BE) and relative areas (A) of the peaks are collected in Table 2. Curve fitting of the Zn2p orbital was not possible because the signal of the spectrum was too low.

The relative concentrations of Sn and O, expressed in at. %, agreed with the formula of SnO_2. The concentration of Zn was 0.2 at. % at the surface of NS Zn/Sn material, and the latter also contained more oxygen than NS Sn: 62.5 at. % versus 60.9 at. %, respectively. Fitting the high-resolution Sn spectra resulted in a single contribution for NS Zn/Sn and NS Sn, assigned to Sn (IV) in SnO_2. Three facts also confirmed that Zn was present in low amount on the NS Zn/Sn surface: (i) the Sn3d and O1s peaks were not shifted to lower BE with respect to the non-doped NS Sn sample, indicating that no oxygen deficiency exists in

the Zn-doped material; (ii) the Sn3d spectrum of NS Zn/Sn presented no shoulder assigned to Zn, thus evidencing the absence of Sn-O-Zn coordination; (iii) the Sn3d and O1s spectra were consistent with each other.

Fig. 3 (a) displays SEM image of NS Zn/Sn in a representative way of what was really deposited on the sensor support. Similar morphology was observed for NS Sn and an image can be seen in Fig. S1 (a) of the supplementary information. NS Sn and NS Zn/Sn were composed of irregular particle agglomerates. Further structural characterization of the prepared nanostructured SnO_2 materials was performed by TEM. Fig. 3 (b) and Fig. S1 (b) display TEM micrographs of NS Zn/Sn and NS Sn, respectively. Both images exhibited agglomerated uniform particles of quasi-spherical morphology with a mean diameter of around 4–5 nm. The doping process seems not modifying the particle size of the nanoparticles. The selected-area electron diffraction (SAED) pattern for the NS Zn/Sn sample is presented in Fig. 3 (c) and contains a set of diffraction rings that were indexed to the (110), (101), (200) and (211) planes of cassiterite, i.e., the rutile-like SnO_2, which is in good agreement with the XRD data. Fig 3 (d) and Fig. S1 (c) showed that no significant chemical contrast was noticed on the high-angle annular dark-field images (HAADF) for Zn-doped SnO_2 material, suggesting a composition as homogeneous as in the non-doped material.

3.2. Gas sensing performances of tin oxide materials

3.2.1 Surface morphology of thick-film gas sensor

Fig. 3 (e) and (f) display SEM images of the resulting NS Sn-based thick film after drop-casting followed by heating at 500°C for 48 h. A fairly uniform film with small grains was

obtained. The thickness of the NS Sn sensitive layer was close to 15 µm. The same morphology and thickness were observed for the Zn-doped SnO_2 film.

3.2.2 Sensors responses in synthetic air (2% RH)

The operating temperature of sensing materials is an important parameter for resistive gas sensors because of its influence on the gas-sensing process [35, 36]. To evaluate the optimum temperature for formaldehyde detection, each sensor was exposed to 262 ppb formaldehyde vapors at a flow rate equal to 100 mL min^{-1} during 5 min at different temperatures ranging from 50 to 500°C. Fig. 4 (a) represents the typical electrical response of the NS Sn sensor at an operating temperature of 260°C. Looking at the linear variation of the normalized conductance ($G/G°$) of the sensor during the first seconds of formaldehyde exposition, information about the reactivity of the gas sensor submitted to formaldehyde vapors can be obtained from the slope. Fig. 4 (b) shows the evolution of the normalized conductance slope plotted versus the sensitive surface temperature for each gas sensor under 262 ppb of formaldehyde.

The optimum temperatures were estimated at 230 and 260°C for NS Zn/Sn and NS Sn sensors, respectively. Therefore, the presence of Zn in NS Zn/Sn sensor lowered the optimum temperature for the detection of formaldehyde.

The detection mechanism of formaldehyde with tin oxide-based gas sensors was discussed in several previous works [27, 37-38]. In brief, when SnO_2 surface is exposed to synthetic air flow, chemisorbed oxygen species are created at the surface of each grain by trapping electrons from the conduction band (c.b.) of SnO_2 according to the successive reactions:

$$O_{2(gas)} \rightarrow O_{2(ads)} \quad (1)$$

$$O_{2(ads)} + e^-_{c.b.} \rightarrow O_2^-{}_{(ads)} \quad (2)$$

$$O_2^-{}_{(ads)} + e^-_{c.b.} \rightarrow 2\,O^-_{(ads)} \quad (3)$$

$$O^-_{(ads)} + e^-_{c.b.} \rightarrow O^{2-}_{(ads)} \quad (4)$$

These reactions induce the formation of a thick space-charge layer, a high intergranular potential barrier, and then a high electrical resistance of the material. Since SnO_2 is an n-type semiconductor and formaldehyde a reducing gas, an oxidation mechanism of formaldehyde molecules occurs at the sensor surface, and then the electrical resistance decreases when exposed to CH_2O:

$$CH_2O_{(gas)} \rightarrow CH_2O_{(ads)} \quad (5)$$

$$CH_2O_{(ads)} + 2O^- \rightarrow CO_{2(gas)} + H_2O_{(gas)} + 2\,e^-_{c.b.} \quad (6)$$

$$CH_2O_{(ads)} + O_2^- \rightarrow CO_{2(gas)} + H_2O_{(gas)} + e^-_{c.b.} \quad (7)$$

This detection mechanism leads to a thinner space-charge layer, a lower intergranular potential barrier and then to an increase of the concentration of electrons in the conduction band of the material. When the formaldehyde vapor is no more present, the sensor is exposed again to synthetic air flow and then the resistance increases again by trapping atmospheric oxygen molecules.

Fig. 4 (c) shows the real-time response curves upon exposure to various concentrations of formaldehyde, from 262 to 8 ppb, diluted in synthetic air. The exposition time and purging time under pure synthetic air between each CH_2O exposition were 5 min and 15 min, respectively. As expected, the amplitudes of the sensor electrical responses gradually decreased when decreasing the formaldehyde concentration. The responses of the SnO_2-

based sensors as a function of the formaldehyde concentration were also measured and plotted in Fig. 4 (d) in order to estimate the detection limit of each gas sensor. The detection limit corresponds to the concentration at which the amplitude of the electrical response was three times higher than the signal / noise ratio (S/N > 3). The NS Zn/Sn sensor exhibited the highest response amplitude under CH_2O in comparison with the NS Sn sensor. The detection limits for formaldehyde were estimated at 8 and 15 ppb for NS Zn/Sn and NS Sn sensors, respectively. The response of each material increased nearly linearly with the formaldehyde concentration. These low limits of detection (LOD), can be attributed first to the high specific surface area of tin oxide materials (177 and 185 $m^2 g^{-1}$ for NS Zn/Sn and NS Sn sensors, respectively), leading to a high amount of adsorbed oxygen and, maybe, to a high permeability for fast adsorption and gas diffusion. Moreover, the small crystallite size of SnO_2-based materials plays an important role in the sensitivity of metal oxide-based gas sensors. In particular, Xu et al. stated that the sensitivity of the sensor remarkably increases when the crystallite size (*D*) of the sensing material is close to - or less than - the double of the thickness of the space-charge layer (*L*) [39]. For SnO_2 material in air, it is admitted that the space-charge layer produced around the surface of the crystallites due to the chemisorbed oxygens is close to 3 nm [40]. In the present study, the average crystallite sizes obtained by XRD for both synthesized material were 3.1 and 3.3 nm for NS Zn/Sn and NS Sn sensors, respectively, i.e., were lower than 2*L*. In that case, the space-charge layer region dominates the whole particle behavior, and the crystallites are almost fully depleted of mobile charge carriers. The energy bands are nearly flat throughout the whole structure of the interconnected grains. There are no significant barriers for inter-crystallite charge transport and then the conductivity is essentially controlled by the inter-crystallite conductivity. Only a few charges acquired from surface reactions can thus produce large

changes of conductivity of the whole structure, so that the crystalline material becomes highly sensitive to ambient gas molecules when its crystallite size is small enough. A schematic model of the effect of CH_2O exposure on SnO_2 material with small grain size is shown in Fig. 5.

From these electrical responses, the response and recovery times were also evaluated for a formaldehyde concentration of 100 ppb (sensor chamber volume and gas flow rate equal to 25 mL and 100 mL min^{-1}, respectively). Those characteristics are important parameters for estimating the performances of a gas sensor. The response and recovery times are expressed as the time needed for the sensor signal to reach 90% of its saturation after applying or switching off formaldehyde in the gas chamber (see again Fig. 4 (a)). The response and recovery times were 70 s and 126 s, respectively, for NS Sn derived sensor while they were reduced to 60 s and 100 s, respectively, for the NS Zn/Sn-derived one. Therefore, the NS Zn/Sn-derived sensor is the most efficient candidate for the detection of very low formaldehyde concentrations in synthetic air. Indeed, it exhibits excellent responses and good linear dependence in a broad range of formaldehyde concentrations (from 8 ppb up to 262 ppb). Beyond the favorable porous nanostructure, these good performances can be explained by the introduction of a small amount of Zn^{2+} during the synthesis of tin oxide material, in comparison to other materials. According to solid-state chemistry [43, 44], the proportion of oxygen vacancies in Zn-doped SnO_2 nanostructures indeed increases, due to the substitution of Sn^{4+} by Zn^{2+}. Owing to more surface oxygen vacancies, more oxygen species can adsorb at the surface of doped SnO_2, thus leading to a further increase of the sensor response.

Table 3 reports some literature data on the gas sensing performances of various tin oxide-based gas sensors towards formaldehyde in synthetic air. The operating temperature

of NS Zn/Sn material (230°C) is comparable with values reported in the literature results, ranging from 160 to 330°C. Although those temperatures are still higher than room temperature, it is worth noticing that the sensor fabricated in the present work exhibits sensing performances one order magnitude higher than those reported in the literature.

The repeatability of the NS Zn/Sn sensor was also studied by testing 100 ppb of formaldehyde four times under the same conditions (5 min exposition time, 230°C and flow rate equal to 100 mL min^{-1}). From Fig. 4 (e), it can be observed that the NS Zn/Sn gas sensor had a good repeatability and stability over the time.

3.2.3 Sensor response in the presence of humidity

The relative humidity in indoor air usually ranges from 30 to 60% [48]. The electrical signal presented in Fig. 4 (f) shows the real-time response of the NS Zn/Sn sensor for various formaldehyde concentrations under 60% RH at 25°C. The latter figure evidences that there is a very strong influence of water in the detection performances of the NS Zn/Sn gas sensor. In the presence of 60% RH, it was indeed no longer possible to reach a LOD as low as 8 ppb. The competitive adsorption of water and formaldehyde at the surface of the metal oxide during the detection process decreased the detection performances with respect to formaldehyde. In these experimental conditions, the LOD was about 50 ppb. However, even if the signal/noise ratio decreased, the results were still better than those reported in the literature, see again Table 3. The outstanding performances of our SnO_2 based sensors are due to both higher A_{BET} and smaller crystallite size, which provide more surface-active sites, may induce larger changes of electrical conductivity of SnO_2, and thus give the sensor a higher response to reducing gases [42, 49].

4. Conclusion

In the present study, two tin oxide materials (NS Zn/Sn, NS Sn) were synthesized using easy and fast hydrothermal methods. Thick-film gas sensors were fabricated by coating commercial interdigitated comb array platforms with each kind of tin oxide, and were then tested for the detection of formaldehyde in synthetic air. It was found that, at 230°C, the nanoflower Zn-doped SnO_2-based sensor exhibited an excellent response, a good linear dependence in a broad range of formaldehyde concentrations (from 8 ppb to 262 ppb), as well as short response/recovery times and a good repeatability over the time. These good sensing performances were mainly attributed to the high specific surface area and the small crystallite size, which was even reduced by the presence of a small amount of Zn in the SnO_2 matrix. Humidity (60% RH at 25°C) was found to have a strong influence on the formaldehyde detection level, although the lowest detection limit in the present experimental conditions remained quite low, close to 50 ppb. However, the obtained performances are in the range of those fixed by the occupational health authorities worldwide for indoor formaldehyde pollution.

ACKNOWLEDGEMENTS

The IJL research team gratefully acknowledges the financial support of the CPER 2007-2013 “Structuration du Pôle de Compétitivité Fibres Grand’Est” (Competitiveness Fibre Cluster), through local (Conseil Général des Vosges), regional (Région Lorraine), national (DRRT and FNADT) and European (FEDER) funds. Part of this work was also supported by CHEERS and TALiSMAN projects (FEDER funds). Dr. Angela Sanchez - Sanchez acknowledges

the University of Lorraine, the Region Lorraine and the CNRS for financing her postdoctoral contract.

References

[1] H. Checkoway, L. D. Dell, P. Boffetta, A. E. Gallagher, L. Crawford, P. SJ Lees, K. A. Mundt, Formaldehyde Exposure and Mortality Risks From Acute Myeloid Leukemia and Other Lymphohematopoietic Malignancies in the US National Cancer Institute Cohort Study of Workers in Formaldehyde Industries. JOEM 57 (2015) 7 785 – 794.

[2] C. Bosetti, J. K. McLaughlin, R. E. Tarone, E. Pira, C. La Vecchia, Formaldehyde and cancer risk: a quantitative review of cohort studies through 2006, Ann Oncol. 19 (2008) 1 29-43.

[3] Shaobin Wang, H.M. Ang, Moses O. Tade, Volatile organic compounds in indoor environment and photocatalytic oxidation: State of the art, Environment International 33 (2007) 694–705.

[4] S. N. Sax, D. H. Bennett, S. N. Chillrud, P. L. Kinney, J. D. Spengler, Differences in source emission rates of volatile organic compounds in inner-city residences of New York City and Los Angeles, Journal of Exposure Analysis and Environmental Epidemiology (2004) 14, 95–109.

[5] T Salthammer, S. Mentese, R. Marutzky, Formaldehyde in the Indoor Environment, Chemical Reviews 110 (2010) 4 2536 – 2572.

[6] AFSSET Working Group on Indoor Air Quality Guideline Values. Indoor Air Quality, Guideline Value Proposals Formaldehyde; AFSSET: Maisons-Alfort Cedex, French, 2007.

[7] C. Mandin, N. Bonvallot, S. Kirchner, M. Keirsbulck, R. Alary, P.-A. Cabanes, F. Dor, Y. Le Moullec, J.-U. Mullot, A.-E. Peel, C. Rousselle, CLEAN-Soil, Air, Water 37 *(*2009) 6, 494-499.

[8] J. Zhang, Z. Qin, D. Zeng, C. Xie, Metal-oxide-semiconductor based gas sensors: screening, preparation, and integration, Phys. Chem. Chem. Phys. 19 (2017) 6313—6329.

[9] S. J. Patil, A. V. Patil, C. G. Dighavkar, K. S. Thakare, R. Y. Barase, S. J. Nandre, N. G. Deshpande, R. R. Ahire, Semiconductor metal oxide compounds based gas sensors: A literature review, Frontiers of Materials Science 9 (2015) 1 14–37.

[10] G. Wolfgang, K.D. Schierbaum, SnO_2 sensors: current status and future prospects, Sens. Actuat. B 26 (1995) 1–12.

[11] T. Oyabu, Sensing characteristics of $Sn0_2$ thin film gas sensor, J. Appl. Phys. 53 (1982) 2785 – 2787.

[12] S. Das, V. Jayaraman, SnO_2: A comprehensive review on structures and gas sensors, Progress in Materials Science 66 (2014) 112-255.

[13]P. T. Moseley, Progress in the development of semiconducting metal oxide gas sensors: a review, Meas. Sci. Technol. 28 (2017) 82001 (15pp).

[14] G.-J. Li, S. Kawi, High-surface-area SnO_2: a novel semiconductor-oxide gas sensor, Materials Letters 34 (1998) 99- 102.

[15] Y.-F. Sun, S.-B. Liu, F.-L. Meng, J.-Y. Liu, Z. Jin, L.-T. Kong, J.-H. Liu, Metal Oxide Nanostructures and Their Gas Sensing Properties: A Review, Sensors 12 (2012) 2610-2631.

[16] C. Wang, L. Yin, L. Zhang, D. Xiang, R. Gao, Metal Oxide Gas Sensors: Sensitivity and Influencing Factors, Sensors 10 (2010) 2088-2106.

[17] A. Mirzaei, S.G. Leonardi, G. Neri, Detection of hazardous volatile organic compounds (VOCs) by metal oxide nanostructures-based gas sensors: A review, Ceramics International 42 (2016) 15119–15141

[18] W. Luo, J. Deng, Q. Fu, D. Zhou, Y. Hu, S. Gong, Z. Zheng, Nanocrystalline SnO_2 film prepared by the aqueous sol–gel method and its application as sensing films of the resistance and SAW H_2S sensor, Sens. Actuat. B 217 (2015) 119–128.

[19] J.M. Correia-Pires, V. Teixeira, J.B. Almeida, Deposition of SnO_2-Based Thin Films By Reactive DC Magnetron Sputtering for Gas Sensing Applications, Nanostructured Materials and Coatings for Biomedical and Sensor Applications, NATO Science Series (Series II: Mathematics, Physics and Chemistry), 102. Springer, Dordrecht, (2003).

[20] D. Liang, S. Liu, Y. Guo, Z. Wang, W. Jiang, C Liu, W. Ding, H. Wang, N. Wang, Z. Zhang, Crystalline size- control of SnO_2 nanoparticles with tunable properties prepared by HNO_3-ethanol assisted precipitation, Journal of Alloys and Compounds 728 (2017) 118-125.

[21] X. Dou, D. Sabba, N. Mathews, L. H. Wong, Y. Ming Lam, S. Mhaisalkar, Hydrothermal Synthesis of High Electron Mobility Zn-doped SnO_2 Nanoflowers as Photoanode Material for Efficient Dye-Sensitized Solar Cells, Chem. Mater. 23 (2011) 3938–3945.

[22] S. Brunauer, P. H. Emmett, E. Teller, Adsorption of Gases in Multimolecular Layers, J. Am. Chem. Soc. 60 (1938) 2 309-319.

[23] M. M. Dubinin, Fundamentals of the theory of adsorption in micropores of carbon adsorbents: Characteristics of their adsorption properties and microporous structures, Carbon 27 (1989) 3 457-467.

[24] Y.-F. Zhao, Y.-P. Sun, X. Yin, G.-C. Yin, X.-M. Wang, F.-C. Jia, B. Liu Effect of Surfactants on the Microstructures of Hierarchical SnO_2 Blooming Nanoflowers and their Gas-Sensing Properties, Nanoscale Res Lett. 13 (2018) 250.

[25] G. Liu, Z. Wang, Z. Chen, S. Yang, X. Fu, R. Huang, X. Li, J. Xiong, Y. Hu, H. Gu, Remarkably enhanced room-temperature hydrogen sensing of SnO_2 nanoflowers via vacuum annealing treatment, Sensors 18 (2018) 949.

[26] D. Meng, D. Liu, G. Wang, Y. Shen, X. San, M. Li, F. Meng, Low-temperature formaldehyde gas sensors based on NiO-SnO_2 heterojunction microflowers assembled by thin porous nanosheets, Sens. and Actuat. B 273 (2018) 10 418-428.

[27] Y. Li, N. Chen, D. Deng, X. Xing, X. Xiao, Y. Wang, Formaldehyde detection: SnO_2 microspheres for formaldehyde gas sensor with high sensitivity, fast response/recovery and good selectivity, Sens. Actuat. B 238 (2017) 264–273.

[28] S. Tian, X. Ding, D. Zeng, S. Zhang, C. Xie, Pore-size-dependent sensing property of hierarchical SnO_2 mesoporous microfibers as formaldehyde sensors, Sens. Actuat. B 186 (2013) 640– 647.

[29] H. Ren, W. Zhao, L. Wang, S. Ok Ryu, C. Gu, Preparation of porous flower-like SnO_2 micro/nano structures and their enhanced gas sensing property, Journal of Alloys and Compounds 653 (2015) 611-618.

[30] K. Xu, D. Zeng, S. Tian, S. Zhang, C. Xie, Hierarchical porous SnO_2 micro-rods topologically transferred from tin oxalate for fast response sensors to trace formaldehyde, Sens. Actuat. B 190 (2014) 585– 592.

[31] C. Gu, Y. Cui, L. Wang, E. Sheng, J.-J. Shim, J. Huang, Synthesis of the porous NiO/SnO_2 microspheres and microcubes and their enhanced formaldehyde gas sensing performance, Sens. Actuat. B 241 (2017) 298-307.

[32] R. Li, S. Chen, , Z. Lou, L. Li, T. Huang, Y. Song, D. Chen, G. Shen, Fabrication of porous SnO_2 nanowires gas sensors with enhanced sensitivity, Sens. Actuat. B 252, (2017) 79-85.

[33] M. Wu, W. Zeng, Q. He, J. Zhang, Hydrothermal synthesis of SnO2 nanocorals, nanofragments and nanograss and their formaldehyde gas-sensing properties, Mat. Sci. Semicon. Proc. 16 (2013) 6 1495-1501.

[34] N. Li, Y. Fan, Y. Shi, Q. Xiang, X, Wang, J. Xu, A low temperature formaldehyde gas sensor based on hierarchical SnO/SnO_2 nano-flowers assembled from ultrathin nanosheets: Synthesis, sensing performance and mechanism, Sens. Act. B 294 (2019) 106-115.

[35] J.F. McAleer, P.T. Moseley, J.O.W. Norris, D.E. Williams, P. Taylor, B.C. Tofield, Tin oxide based gas sensors, Materials Chemistry and Physics 17 (1987) 577-583.

[36] D. Kohl, Surface processes in the detection of reducing gases with SnO_2-based devices, Sens. Actuat. B 18 (1989) 71-113.

[37] S. Li, Y. Liu, Y. Wu, W. Chen, Z. Qin, N. Gong, D. Yu, Highly sensitive formaldehyde resistive sensor based on a single Er-doped SnO_2 nanobelt, Physica B 489 (2016) 33–38.

[38] C. Gu, Y. Cui, L. Wang, E. Sheng, J.-J Shim, J. Huang, Synthesis of the porous NiO/SnO_2 microspheres and microcubes and their enhanced formaldehyde gas sensing performance, Sens. Actuat. B 241 (2017) 298–307.

[39] C. Xu, J. Tamaki, N. Miura, N. Yamazoe, Grain size effects on gas sensitivity of porous $Sn0_2$-based elements, Sens. Actuat. B 3 (1991) 147-155.

[40] N. Yamazoe, New approaches for improving semiconductor gas sensors, Sens. Actuat. B 5 (1991) 7-19.

[41] Y.-F. Sun, S.-B. Liu, F.-L. Meng, J.-Y. Liu, Z. Jin, L.-T. Kong, J.-H. Liu, Metal Oxide Nanostructures and Their Gas Sensing Properties: A Review, Sensors 12 (2012) 2610-2631.

[42] M. E. Franke, T. J. Koplin, U. Simon, Metal and Metal Oxide Nanoparticles in Chemiresistors: Does the Nanoscale Matter?, Small, 2 (2006) 36-50.

[43] Y. Guan, D. Wang, X. Zhou, P. Sun, H. Wang, J. Ma, G. Lu, Hydrothermal preparation and gas sensing properties of Zn-doped SnO_2 hierarchical architectures, Sens. Actuat. B 191 (2014) 45– 52.

[44] X. Dinga, D. Zenga, C. Xie, Controlled growth of SnO_2 nanorods clusters via Zn doping and its influence on gas-sensing properties, Sens. Actuat. B 149 (2010) 336–344.

[45] J. Yang, S. Wang, R. Dong, L. Zhang, Z. Zhu, X. Gao, One-potsynthesis of SnO_2 hollow microspheres and their formaldehyde sensor application, Materials Letters 184 (2016) 9–12.

[46] I. Castro-Hurtado, J. Herrán, G. Ga Mandayo, E. Castaño, SnO_2-nanowires grown by catalytic oxidation of tin sputtered thin films for formaldehyde detection, Thin Solid Films 520 (2012) 4792–4796.

[47] H. Yu, T. Yang, Z. Wang, Z. Li, B. Xiao, Q. Zhao, M. Zhang, Facile synthesis cedar-like SnO_2 hierarchical micro-nanostructures with improved formaldehyde gas sensing characteristics, Journal of Alloys and Compounds**,** 724 **(**2017**)** 121-129**.**

[48] A.V. Arundel, E.M. Sterling, J.H. Biggin, T.D. Sterling, Indirect health effects of relative humidity in indoor environments, Environ. Health Persp. 65 (1986) 351-361.

[49] A. Rothschild, Y. Komem, The effect of grain size on the sensitivity of nanocrystalline metal-oxide gas sensors, Journal of Applied Physics 95 (2004) 6374-6380.

Figure

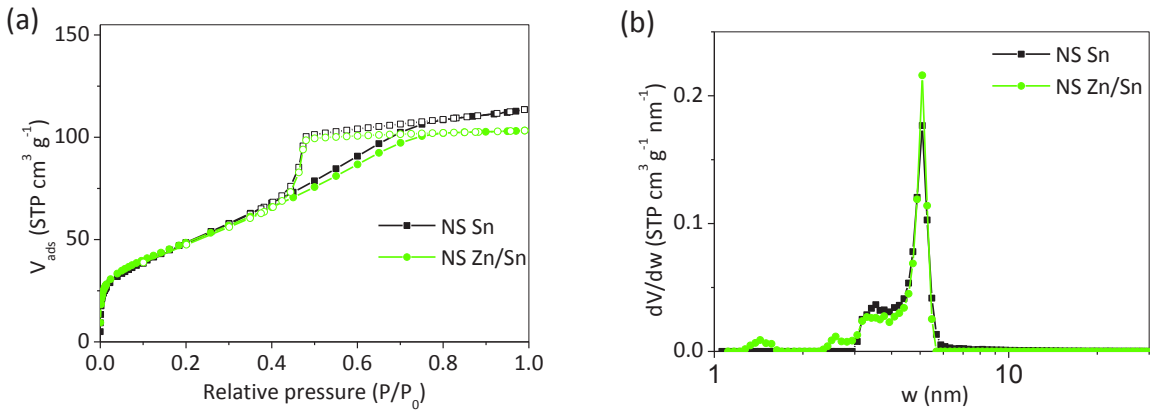

Fig. 1: (a) Nitrogen adsorption (full symbols) – desorption (empty symbols) isotherms of the materials measured at -196°C; (b) Pore size distributions (PSDs) obtained by applying the NLDFT method to the data shown in (a).

Figure

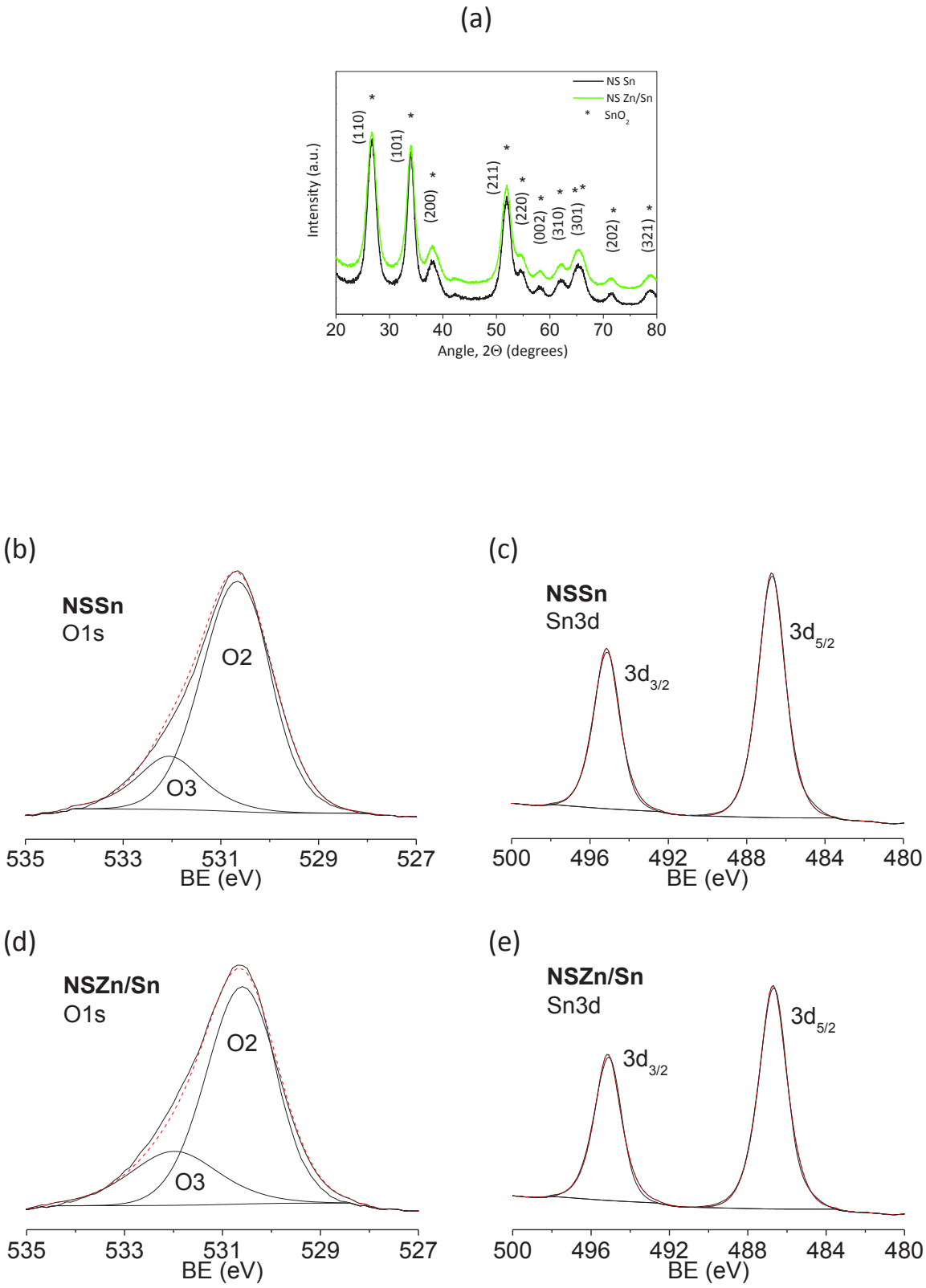

Fig. 2: (a) Wide-angle XRD profiles, (b and d) O1s and (c and e) Sn3d high-resolution XPS spectra of the studied materials.

Figure

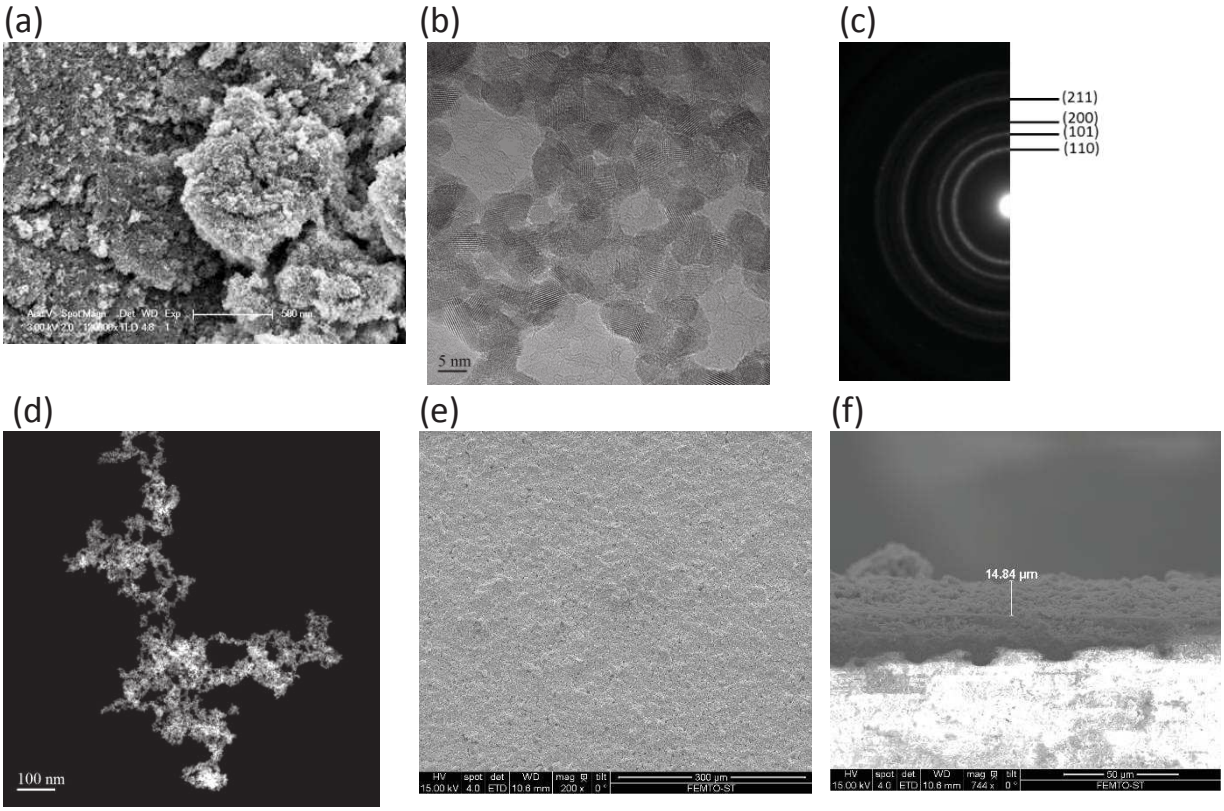

Fig. 3: (a) SEM image, (b) BF-TEM image, (c) SAED pattern and (d) HAADF-STEM image of the nanostructured Zn-doped SnO_2. Top (e) and side (f) views by SEM of the NS Sn-based thick film produced by the drop-casting process.

Figure

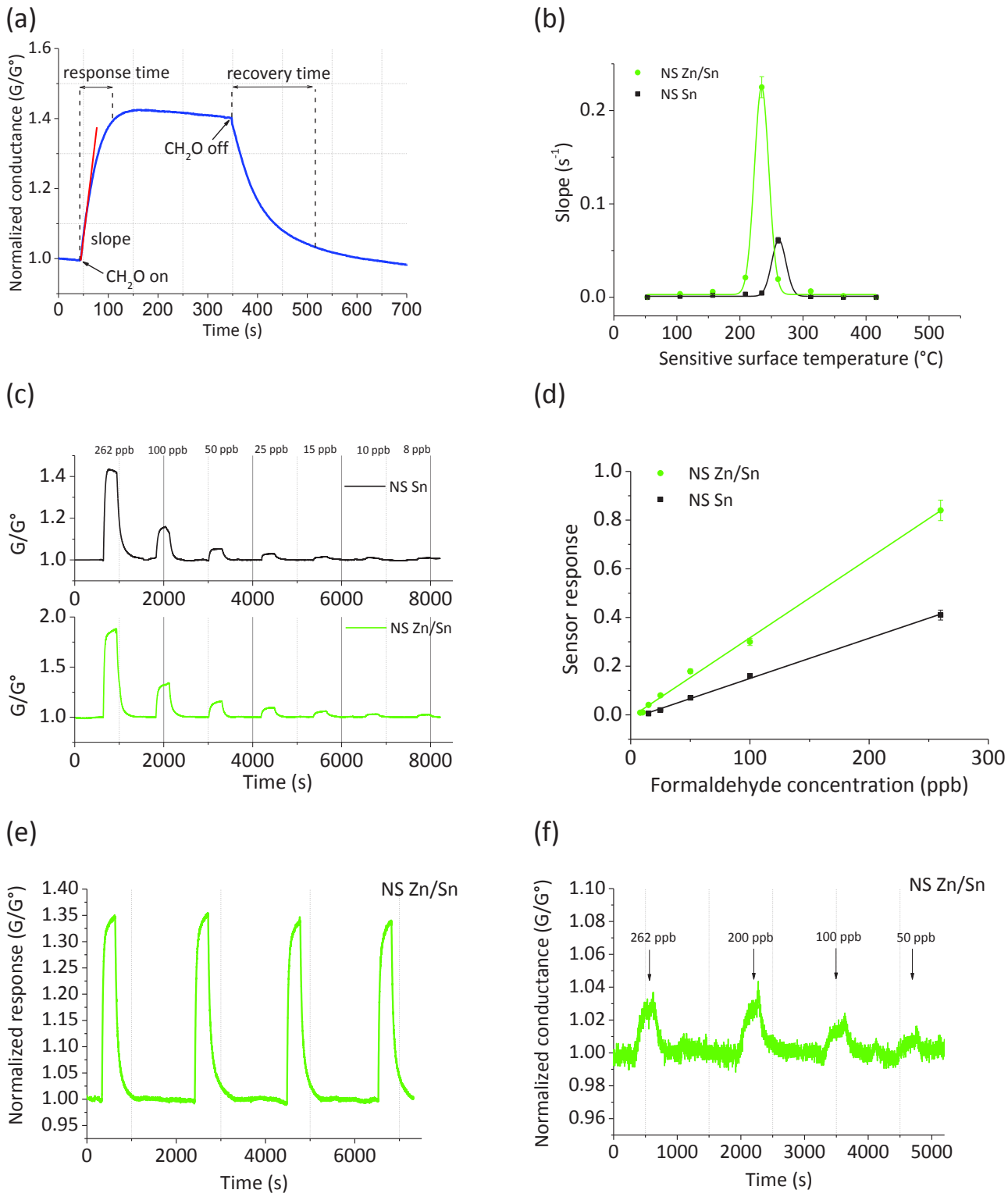

Fig. 4: (a) Dynamic response of the NS Sn sensor at an operating temperature of 260°C; (b) evolution of the normalized conductance slopes under 262 ppb of formaldehyde; (c) real-time responses of each sensor for various formaldehyde concentrations (sensing temperatures equal to 260°C and 230°C for NS Sn and NS Zn/Sn, respectively); (d) responses of the SnO_2-based gas sensors as a function of the formaldehyde concentration; (e) repeatability of the NS Zn/Sn gas sensor under 100 ppb of formaldehyde (sensing temperature equal to 230°C); (f) real-time responses of the NS Zn/Sn sensor for various formaldehyde concentrations under 60% RH at 25°C (sensing temperature equal to 230°C). For all tests, 5 min exposition time and 100 mL min^{-1} flow rate were applied.

Figure

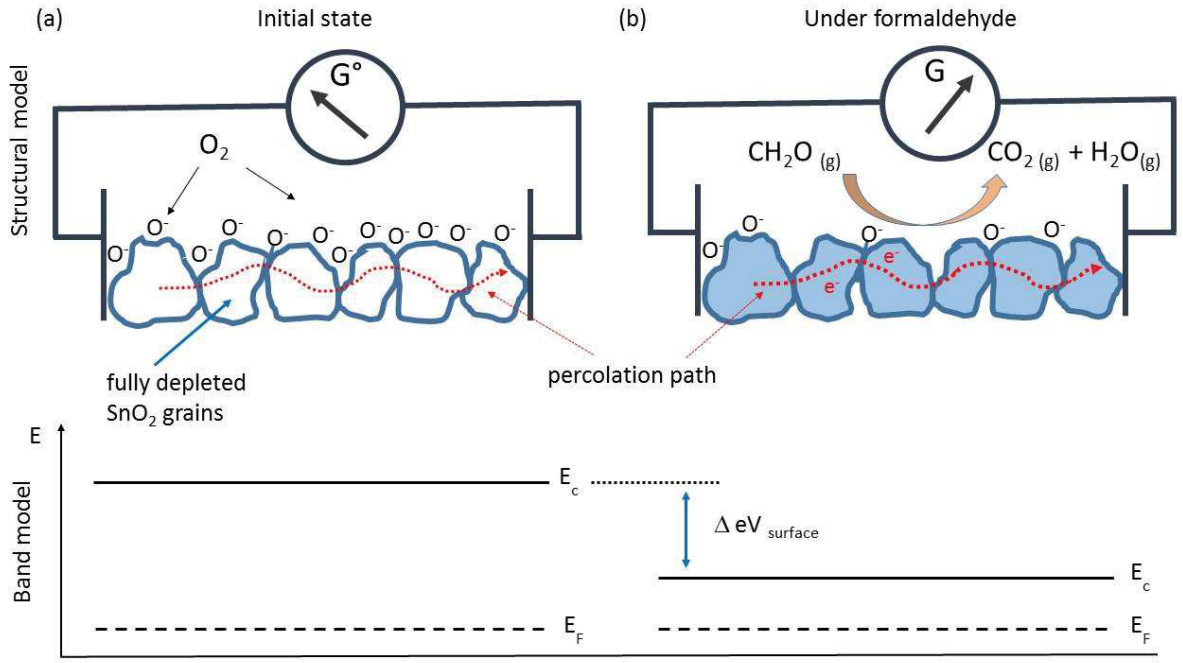

Fig. 5: Structural and band model for a SnO_2 material with crystallite size lower than the double of the thickness of the space-charge layer: (a) initial state under synthetic air and (b) effect of formaldehyde on the position of the conduction band. E_c and E_F denote the energy of the conduction band and Fermi level, respectively, while $eV_{surface}$ denotes the potential barrier (adapted from Refs. [41, 42]).

Table

Table 1: textural properties of nanostructured SnO_2 materials for sensing applications.

Materials	Average crystallite size (nm)	A_{BET} (m^2/g)	Ref.
NS Sn	3.3	185	This study
NS Zn/Sn	3.1	177	This study
Zn doped SnO_2 nanoflowers		10	[21]
SnO_2 blooming nanoflowers	20	15.5-38.4	[24]
SnO_2 nanoflowers	350	27.6-29.8	[25]
NiO-SnO_2 heterojunction microflowers	10-20	38-39	[26]
SnO_2 microspheres	8	64	[27]
SnO_2 mesoporous microfibers	2.5-8.5	58-101	[28]
Porous flower-like SnO_2	6.3	67	[29]
Hierarchical porous SnO_2 micro-rods	5-10	11	[30]
Porous NiO/SnO_2 microspheres and microcubes	7.5-11.6	38.5-61.5	[31]
Porous SnO_2 nanowires	n.a.	38	[32]
SnO_2 nanocorals	200-300	23.2	[33]
SnO/SnO_2 nanoflowers	9-11	25.3-28.1	[34]

n.a.: not available

Table

Table 2: Surface chemical composition data obtained from XPS.

Sample	Surface concentration (at. %)			Binding energies (eV) and relative peak areas (%)						
				O1s peak			$Sn3d_{5/2}$		$Sn3d_{3/2}$	
	O	Sn	Zn	O1	O2	O3	II(1)	II(2)	II(1)	II(2)
NS Sn	60.9	39.1	-	-	530.7 (81.7)	532.2 (18.3)	486.7 (61.8)	-	495.1 (38.2)	-
NS Zn/Sn	62.5	37.3	0.2	-	530.6 (77.2)	531.9 (22.9)	486.7 (62.0)	-	495.1 (38.0)	-

Table

Table 3: Comparison of the sensing performances of various SnO_2-based gas sensors for the detection of formaldehyde in synthetic air.

Materials	Optimum T (°C)	LOD (ppb)	RH (%)	Ref.
NS Sn	260	15	2	This study
NS Zn/Sn	230	8	2	This study
		50	60	
SnO_2 microspheres	200	1000	25-30	[27]
SnO_2 hollow microspheres	300	1000	n.a.	[45]
SnO_2 mesoporous microfibers	150	50	n.a.	[28]
Porous flower-like SnO_2	240	110	n.a.	[29]
Hierarchical porous SnO_2 micro-rods	330	50	n.a.	[30]
SnO_2 nanowires	270	20	n.a.	[46]
Porous SnO_2 nanowires	380	1000	n.a.	[32]
SnO_2 nanocorals	300	2000	n.a.	[33]
Cedar-like SnO_2 nanostructures	200	1000	n.a.	[47]
NiO-SnO_2 microflowers	100	100	n.a.	[26]
SnO/SnO_2 nanoflowers	120	1000	n.a.	[34]

n.a.: not available

Supplementary Material

Click here to download Supplementary Material: Supplementary information.docx